2017

# Effects of rain and soil moisture on background neutron measurements with the SuperMISTI neutron array

Anthony L. Hutcheson
*U.S. Naval Research Laboratory*, anthony.hutcheson@nrl.navy.mil

J. Eric Grove
*U.S. Naval Research Laboratory*

Lee J. Mitchell
*U.S. Naval Research Laboratory*

Bernard F. Phlips
*U.S. Naval Research Laboratory*

Richard S. Woolf
*U.S. Naval Research Laboratory*

***See next page for additional authors***

Radiation Measurements 99 (2017) 50–59

Contents lists available at ScienceDirect

Radiation Measurements

journal homepage: www.elsevier.com/locate/radmeas

# Effects of rain and soil moisture on background neutron measurements with the SuperMISTI neutron array

Anthony L. Hutcheson*, J. Eric Grove, Lee J. Mitchell, Bernard F. Phlips, Richard S. Woolf, Eric A. Wulf

*U.S. Naval Research Laboratory, 4555 Overlook Avenue, SW, Washington, DC, 20375, United States*

## HIGHLIGHTS

- Variations in local neutron background due to soil moisture changes were observed.
- Neutron rate variations were modeled using basic climatological data.
- Statistical qualities of the models' predictions were compared.

## ARTICLE INFO

*Article history:*
Received 21 October 2016
Received in revised form
30 January 2017
Accepted 20 March 2017
Available online 22 March 2017

*Keywords:*
Neutron background
Gas proportional detectors
Soil moisture

## ABSTRACT

Background neutron measurements were recorded for approximately two months at Camp Blanding, FL, with a large array of moderated gas proportional detectors and EJ-309 liquid scintillator detectors. The variations in the local neutron background rate were on the order of 10% and were observed to be primarily due to the changing level of moisture in the local soil due to precipitation and evaporation. Simple models were constructed based only on very basic climatological information and were able to reproduce the major variations in our measured neutron counts with time. These simple models compare favorably to the more-complex modified Penman equation developed for the California Irrigation Management Information System. An accurate model to describe local neutron background variations based on easily measured climatological data would be invaluable to provide corrections for stationary neutron monitors.

Published by Elsevier Ltd.

## 1. Introduction

In the summer of 2014, the Naval Research Laboratory (NRL) conducted measurements at the International Center for Lightning Research and Testing (ICLRT) at Camp Blanding, FL, with the goal of studying ionizing radiation associated with lightning events (Grove et al., 2014). Because of the unpredictable nature of storms and associated natural lightning, the radiation detection system was operated nearly continuously during the entire deployment. As a result, incidental data were taken for weeks of background neutron measurements with a large array of neutron detectors. To observe the local effect of soil moisture on the measured background rate, these data were corrected for fluctuations in the cosmic-ray-induced neutron rate and variations due to local barometric pressure.

## 2. Background

It has long been known that the intensity of cosmic-ray neutrons at ground level is dependent on the moisture content of the surrounding soil (Hendrick and Edge, 1966). This effect has been exploited by researchers to attempt to measure average soil moisture by utilizing relatively small (~130 $cm^3$) gas proportional counters (Zreda et al., 2012) as well to search for water on Earth's moon (Mitrofanov et al, 2010) and on Mars (Litvak et al, 2008). Conversely, this effect can introduce significant variations into the neutron background measured by stationary neutron detectors that are employed to detect illicit trafficking of special nuclear material or monitor areas (e.g., nuclear reactor facilities) that may potentially be exposed to unwanted neutron radiation. Variations in the neutron background due to the moisture content of the surrounding soil can be larger than expected statistical fluctuations by more than a factor of 50. Such large variations require that detectors either have higher thresholds for detection, which

* Corresponding author.
*E-mail address:* anthony.hutcheson@nrl.navy.mil (A.L. Hutcheson).

http://dx.doi.org/10.1016/j.radmeas.2017.03.029
1350-4487/Published by Elsevier Ltd.

negatively impacts the sensitivity of the detector, or live with a high false-alarm rate. Maximizing the detection sensitivity of these monitors requires a robust method to correct for these background variations.

## 3. Experimental setup

### 3.1. Location

The ICLRT is situated in the Trail Ridge physiographic region of Clay County, FL (Natural Resource Conservation Service, 1989). Soil surveys of the region describe the geologic materials as comprising primarily quartz sand, clay, and shell material. Much of the area has been mined for titanium minerals (ilmenite, leucoxene, and rutile) and zircon. The summer months (June through September) see the heaviest rainfall of the year, with heavy afternoon thunderstorms capable of producing two to three inches of rainfall over a period of one to two hours. The average relative humidity is approximately 75%; during summer months, the average daily temperature is approximately 26.7 °C (80 °F), with an average daily maximum temperature of 32.2 °C (90 °F).

### 3.2. Detectors

The neutron-detection variation of the SuperMISTI (Mobile Imaging and Spectroscopic Threat Identification) detection system (Hutcheson et al., 2015) was deployed to measure neutrons associated with lightning events. This SuperMISTI system (Hutcheson et al., 2014) comprises different subsystems housed in 20-ft refrigerated International Organization for Standardization (ISO) containers and powered entirely by clip-on diesel generators; see Fig. 1. The refrigeration system provides temperature and humidity control for the housed detectors and electronics. Each SuperMISTI container is equipped with a pair of global positioning system (GPS) receivers to determine location, speed, and orientation. On-board electronics are additionally protected from power fluctuations by a rack-mounted uninterruptible power supply (UPS) and can be accessed and controlled via an external Ethernet port on the front of the ISO container. The particular subsystem used for this measurement campaign, the neutron-detection subsystem, comprises a suite of moderated gas proportional counters and EJ-309 organic liquid scintillators; see Fig. 2. For the purposes of this report, the primary focus will be the array of gas proportional counters, which comprises 24 moderated $BF_3$ detectors (Ø11.43 cm × 182.88 cm; 0.92 atm) and six moderated $^3He$ detectors (Ø14.73 cm × 64.01 cm; 2.65 atm). However, as the gas proportional counters give no spectroscopic information, data from the liquid scintillator array is used to observe the neutron pulse-height spectra above 0.5 MeV.

The $BF_3$ array is installed as four modules of six detectors. Each module comprises a dimensional lumber frame that defines six padded cells in which the $BF_3$ tubes are housed. Each tube is surrounded by high-density polyethylene (HDPE) moderator: 5.08 cm on the outward-facing side of the module, 3.81 cm on the inward-facing side of the module, and 2.54 cm on all remaining sides. A photograph of one of these modules (with the interior-facing HDPE moderator removed) is shown in Fig. 3.

**Fig. 1.** External photograph of SuperMISTI detection system.

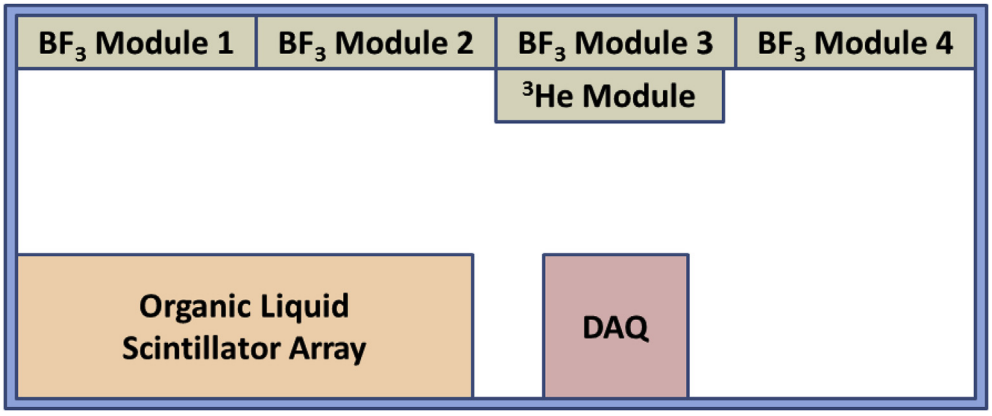


**Fig. 2.** Interior layout of SuperMISTI neutron-detection system. (Top view. Left is toward rear doors of the ISO container.)


**Fig. 3.** Interior view of one of the $BF_3$ modules with the inward-facing moderation removed.

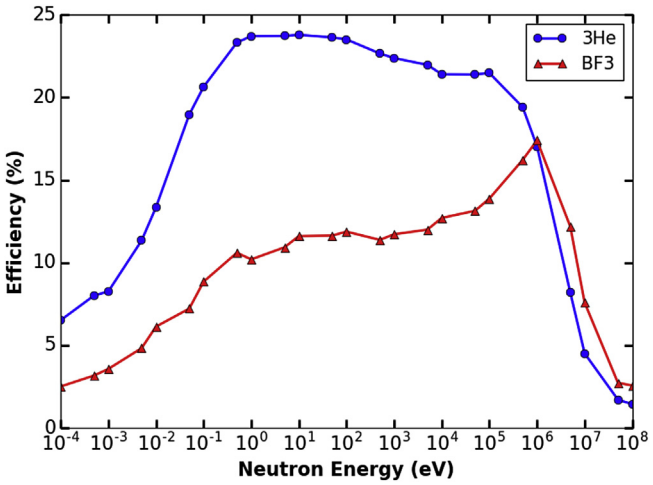


**Fig. 4.** Simulated intrinsic efficiency of the $^3$He (blue circles) and $BF_3$ (red triangles) modules. For these efficiency calculations, the flux through the entire module volume was considered. (For interpretation of the references to colour in this figure legend, the reader is referred to the web version of this article.)

The $^3$He array is installed in a module similar to those that house the $BF_3$ array. However, there is no dimension lumber frame for this module; due to its smaller size, the walls of the module are simply constructed of 2.54-cm-thick HPDE. As a result, the $^3$He tubes are moderated on all sides by 2.54 cm of HDPE.

The intrinsic efficiency of each module type was simulated in Geant4 (Agonstinelliet al, 2003) with the SWORD integrated modeling software (Novikova et al., 2006). For this efficiency calculation, the entire volume of each module was considered when determining the flux; however, only energy deposited in the active volume of the proportional counters was used to determine detection. The resulting efficiency curves are shown in Fig. 4. The $^3$He module exhibits a nearly flat response to neutrons in the energy range from 0.1 eV to 1 MeV; the response for the $BF_3$ module increases with energy until it peaks at approximately 1 MeV and decreases thereafter.

The liquid scintillator detector array comprises 48 EJ-309 liquid scintillator detectors (15.2 cm × 15.2 cm × 15.2 cm) coupled to ETL 9390 KB photomultiplier tubes (PMTs); the detectors are arranged in a 6 × 8 array with a pitch of 18.4 cm.

The SuperMISTI container was deployed in a large, grassy field at the ICLRT facility. Sand was deposited on a small (approximately 200 m$^2$) area of the field to level the region sufficiently to park the container easily; see Fig. 5. In addition, a Davis Vantage Pro2 wireless weather station was collocated with the SuperMISTI container for the entirety of this measurement campaign.

### 3.3. Data acquisition system (DAQ)

High voltage is applied and pulse signals are obtained from the single SHV input/output of each $BF_3$ detector via ORTEC 142AH preamplifiers; the output pulses from the preamps are input into Mesytec MSCF-16 shaping amplifiers followed by a Mesytec MADC-32 peak sensing ADC. Each of the $^3$He detectors provides two output signals: a TTL trigger signal and a Gaussian-shaped amplitude signal that was input directly into a Mesytec MADC-32. The ADC data buffers are time tagged with the system clock of the readout computer, which is synchronized with the onboard GPS system using the Network Time Protocol (NTP). To provide accurate time stamps for each event, each ADC is provided a 10-MHz external oscillator signal from a Stanford Research Systems FS725 rubidium oscillator, which in turn is trained to the pulse-per-second (PPS) signal from the onboard GPS module.

The output signals from each PMT are processed via Struck SIS3316 16-channel VME flash ADCs. These 14-bit modules have a 250-MHz sampling rate and allow the user to utilize pulse shape discrimination (PSD) techniques to separate fast neutron events from those produced by incident gammas. Pulse height thresholds and gains were adjusted to provide a dynamic range of neutron energies of approximately 0.5–3.75 MeV. Three flash ADCs are necessary to handle 47 of the detectors as well as a PPS signal from the onboard GPS module; one detector was necessarily omitted from the ADCs to make room for the PPS and was reserved as a spare. The ADCs share a 250-MHz clock that is generated on the master SIS3316 board from the GPS-trained 10-MHz rubidium oscillator and distributed to the remaining three modules. These time markers provide a way to correlate the timing of the flash ADC system to that of the Mesytec MADC system used for the gas proportional array as well as to the slow-logged, peripheral data such as weather station data, onboard temperature, and GPS coordinates.

## 4. Data

Data were recorded nearly continuously from June 23 to August 22; only three significant gaps in the data exist. The largest gap, spanning July 12 to July 16, resulted from a mechanical failure of the container's clip-on generator. Two smaller gaps, occurring on July 7 and July 18, were due to minor system maintenance tasks that required the system to be powered down. The resulting raw neutron counts measured by the system are shown in Fig. 6. The data from only 18 of the 24 $BF_3$ detectors (effectively, three of the four modules) were used for this plot due to occasional noisy periods that appeared in the remaining six detectors; we believe this

**Fig. 5.** The SuperMISTI container deployed at the ICLRT.

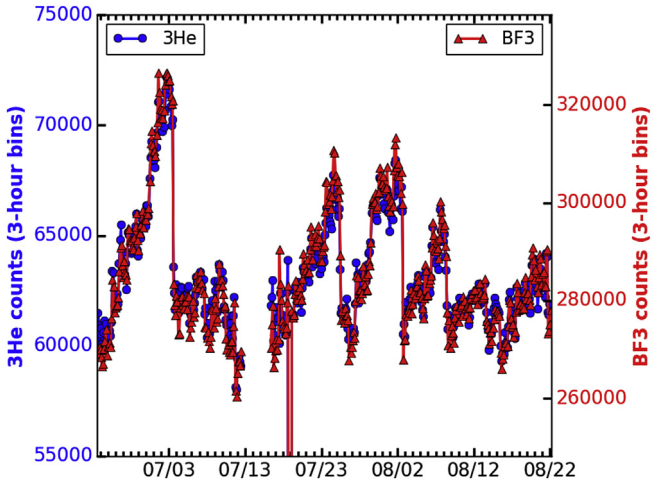


**Fig. 6.** Raw counts (in 3-hour bins) for the $^3$He (blue circles) module and three $BF_3$ (red triangles) modules. The large data gap from July 12 to July 16 is due to a period of generator failure and repair; smaller gaps on July 7 and July 18 are due to minor system maintenance. (For interpretation of the references to colour in this figure legend, the reader is referred to the web version of this article.)

noise to be due to insufficient vibrational isolation of those detectors from the rest of the container. Fig. 7 shows four of the data products obtained from the Davis weather station; the atmospheric pressure (units: in Hg = 3386 Pa), the relative humidity, and the rainfall rate (units: in/h = 25.4 mm/h) are shown in 1-minute bins, whereas the solar irradiance (units: W/m$^2$) is shown in 24-h bins.

The raw neutron counts were then corrected for variations in the cosmic-ray neutron flux and in the atmospheric pressure. To correct for the neutron flux, data were extracted from the Neutron Monitor Database (NMDB) (Neutron Monitor Database) for Newark, New Jersey (39.68° N, 75.75° W), a station with a sufficiently similar longitude (within 2%) to the ICLRT (29.94° N, 82.04° W) such that diurnal variations in the cosmic-ray flux at the two locations should be approximately in phase. The relative deviations from the mean measured neutron counts were calculated for this station and used to correct our raw neutron counts; these relative deviations are shown in Fig. 8.

Corrections for local pressure fluctuations were calculated using the atmospheric pressure measured by the collocated weather station with the well-known relation

$$C = C_0 \cdot e^{-\beta \cdot (P - P_0)} \quad (1)$$

where $C$ is the neutron counts, $P$ is the atmospheric pressure, and $\beta$ is the barometric coefficient. For this correction, the value of $\beta = 0.7629$ %/mbar was obtained from the online Athens Cosmic Ray Station tool (Paschalis et al.).

The effects of the pressure and cosmic-ray-neutron-rate corrections on the raw $BF_3$ neutron counts are shown in Fig. 9; analogous effects are seen for the raw $^3$He neutron counts. The effects of these corrections are relatively small compared to the large variations in the measured neutron count rate; the mean correction is approximately 1%, with a maximum correction of approximately 4%. Fig. 10 shows the corrected $^3$He and $BF_3$ neutron counts with periods of rainfall highlighted in yellow (for less than 0.5″ total rainfall) and green (for greater than or equal to 0.5” total rainfall). Neutron counts fall sharply during significant rainfall and increase slowly between rainfall events. This behavior strongly implies that the dominant cause of the variability in the measured neutron count rate is the level of moisture in the surrounding soil.

To compare the neutron energy spectra above 0.5 MeV before and after a significant rain event, neutron data from the liquid scintillator array were analyzed for two five-minute periods on July 25. On that day, a rain event occurred that resulted in approximately 0.9 inches of rainfall and a corresponding decrease of approximately 9% in the neutron rate measured by the gas proportional array. The spectra of energy deposited in the liquid scintillator array before (shown in blue circles) and after (shown in red -triangles) the rain event are shown in Fig. 11. Despite the significant rainfall, the neutron spectra above 0.5 MeV are virtually identical. This result would indicate that the bulk of the effect seen in the gas proportional array is in neutrons with energies less than 0.5 MeV.

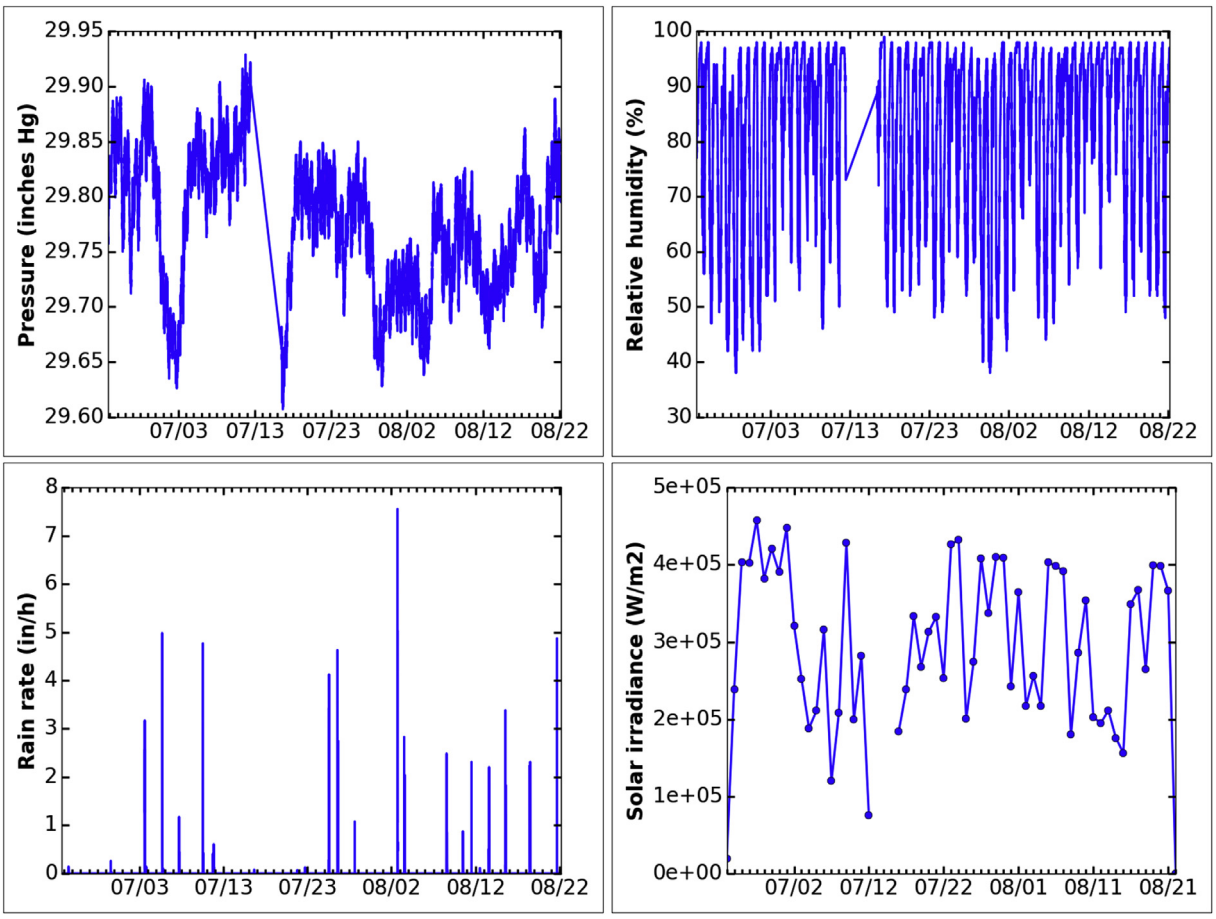


**Fig. 7.** Data recorded by the Davis Vantage Pro2 weather station: (top left) atmospheric pressure, (top right) relative humidity, and (bottom left) rainfall rate in 1-minute bins and (bottom right) solar irradiance in 24-h bins.

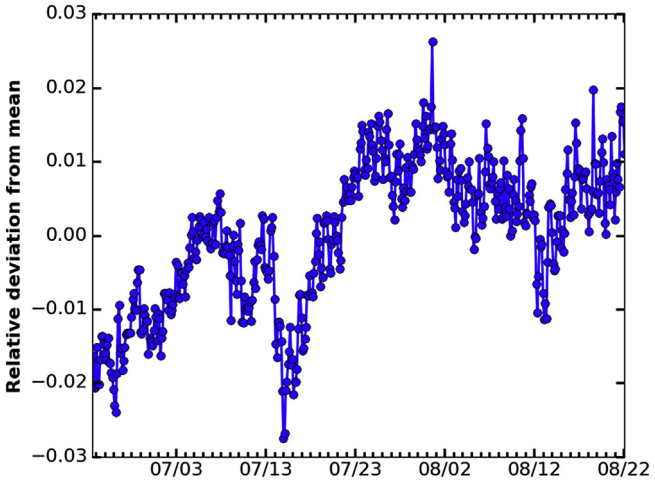


**Fig. 8.** Relative deviation from mean cosmic-ray neutron counts as reported at the NMDB station in Newark, NJ. Data is shown in 3-hour bins.

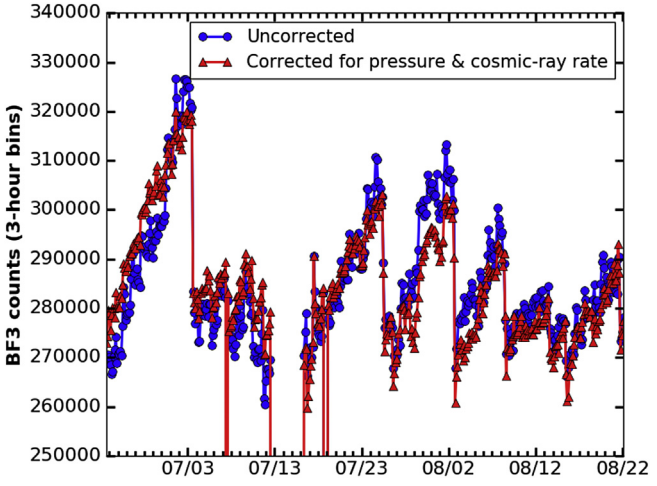


**Fig. 9.** $BF_3$ counts in 3-hour bins: (blue circles) raw counts and (red triangles) counts corrected for variations in both the pressure and the cosmic-ray neutron rate. (For interpretation of the references to colour in this figure legend, the reader is referred to the web version of this article.)

## 5. Model

To model the effect of soil moisture on the measured neutron accounts, we assume that the rate of change of the neutron counts $C$ with respect to the soil moisture $m$ is directly proportional to the soil moisture, resulting in the following exponential relationship:

$$C(m) = C_0 \cdot e^{-a_0 \cdot m} \tag{2}$$

where $C_0 \equiv C(m = 0)$.

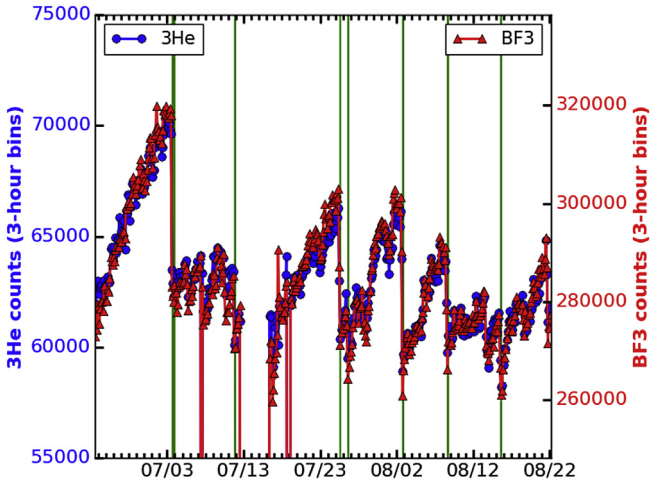


**Fig. 10.** Corrected $^3$He (blue circles) and $BF_3$ (red triangles) counts with periods of rain with greater than or equal to 0.5″ rainfall highlighted in green. (For interpretation of the references to colour in this figure legend, the reader is referred to the web version of this article.)

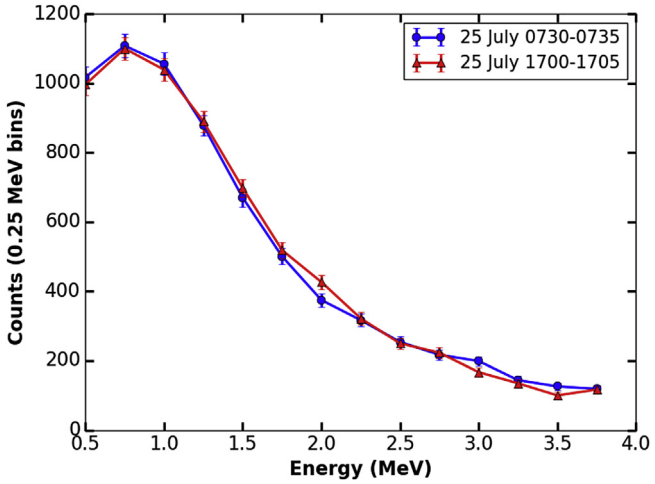


**Fig. 11.** Spectra of energy deposited in the liquid scintillator array by fast neutrons prior to (blue circles) and after (red triangles) the July 25 rain event. (For interpretation of the references to colour in this figure legend, the reader is referred to the web version of this article.)

### 5.1. Model A: rainfall and evaporation

For a very simple initial model for $m(t)$, let us assume that $\frac{dm}{dt}$ depends only on the major source term – the rainfall rate $R(t)$ – and an evaporation term. Evaporation is dependent on the amount of available energy to convert the soil moisture into vapor, and the largest energy source in most cases is the solar irradiance $S(t)$. Therefore, our model is as follows:

$$\frac{dm}{dt} = a_1 \cdot R(t) - a_2 \cdot S(t) \tag{3}$$

$$m(t) = m_0 + a_1 \int_0^t R\left(t'\right)dt' - a_2 \int_0^t S\left(t'\right)dt' \tag{4}$$

where $m_0 \equiv m(t=0)$. By substituting Equation (4) into Equation (2) and consolidating constant terms, we arrive at the following expression:

$$C(t) = k_0 \cdot e^{-k_1 \int_0^t R\left(t'\right)dt' + k_2 \int_0^t S\left(t'\right)dt'} \tag{5}$$

### 5.2. Model B: saturation and dehydration effects

A more realistic complex model assumes a saturation level $m_{max}$ above which the soil can accept no more moisture from the rain. Additionally, the model should account for the fact that soil moisture can never be a negative number. The simplest way to integrate these concepts is to introduce two Heaviside step functions $\theta(m - m_{max})$ and $\theta(m)$:

$$\frac{dm}{dt} = a_1 \cdot R(t) \cdot \theta(m - m_{max}) - a_2 \cdot S(t) \cdot (1 - \theta(m)) \tag{6}$$

The solution to this first-order differential equation must be approximated numerically. Using the Euler method, if we assume constant time bins with width $\Delta t$ and denote $t_n \equiv n \cdot \Delta t$,

$$m(t_n) = m_0 + \Delta t \cdot \sum_{i=0}^{n-1} \frac{dm}{dt}(t_i,\ m(t_i)) \tag{7}$$

Let us further define the unitless quantity $M \equiv \frac{m}{m_{max}}$. Then, substituting and consolidating constants,

$$C(t_n) = C_0 \cdot e^{-k_0 \cdot M(t_n)} \tag{8}$$

$$M(t_n) = M_0 + \Delta t \cdot \sum_{i=0}^{n-1} [k_1 \cdot R(t_i) \cdot \theta(1 - M(t_i)) - k_2 \cdot S(t_i) \cdot (1 - \theta(M(t_i)))] \tag{9}$$

### 5.3. Model C: CIMIS evapotranspiration

A more complex model can be achieved by utilizing the modified Penman equation (Penman, 1948) developed for the California Irrigation Management Information System (CIMIS) (Snyder and Pruitt, 1985) to describe the potential evapotranspiration. This equation takes as inputs the mean temperature, atmospheric pressure, wind speed, solar radiation, and relative humidity; a more detailed discussion of this calculation can be found in the Appendix of this work. By replacing the solar radiation term $S(t)$ with the potential evapotranspiration term $E(t)$ in Equation (9):

$$M(t_n) = M_0 + \Delta t \cdot \sum_{i=0}^{n-1} [k_1 \cdot R(t_i) \cdot \theta(1 - M(t_i)) - k_2 \cdot E(t_i) \cdot (1 - \theta(M(t_i)))] \tag{10}$$

## 6. Results

Figs. 12–14 show the corrected $BF_3$ counts (shown in blue circles) overlaid with least-squares fits of Models A (shown in red triangles), B (shown in green squares), and C (shown in magenta diamonds). Because these models depend on the integral of the rainfall and solar irradiance or potential evapotranspiration, the data chosen for this fit was the longest uninterrupted period of this

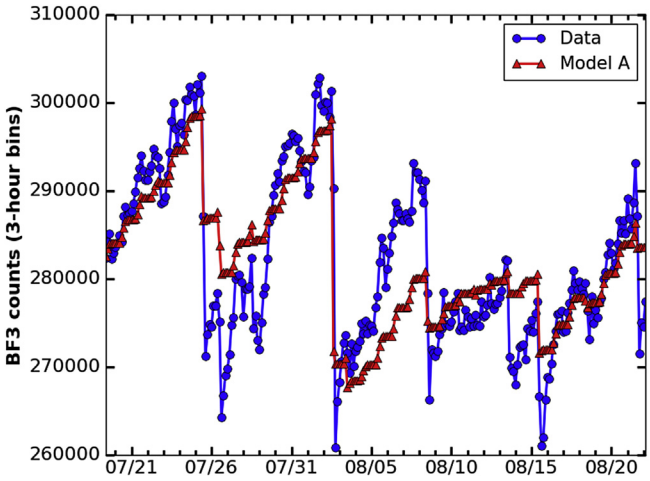


**Fig. 12.** Corrected counts (blue circles) and Model A (red triangles) fit to data for longest uninterrupted data set for the $BF_3$ modules. (For interpretation of the references to colour in this figure legend, the reader is referred to the web version of this article.)

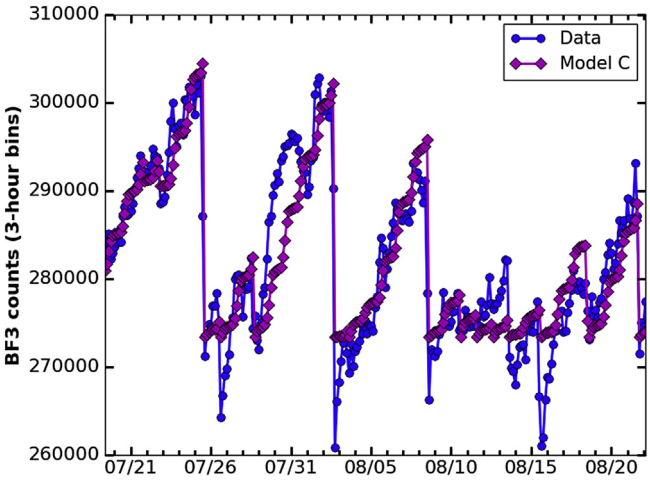


**Fig. 14.** Corrected counts (blue circles) and Model C (magenta diamonds) fit to data for longest uninterrupted data set for the $BF_3$ modules. (For interpretation of the references to colour in this figure legend, the reader is referred to the web version of this article.)

measurement campaign (July 19 to August 22). Although Model A is able to grossly approximate the major structural features of the data, it is clear that the introduction of the saturation and dehydration terms into the model is necessary to reproduce the data features well. Qualitatively, Models B and C produce relatively similar results for this data set. The two more complex models do an excellent job of reproducing all the major data features except two: the continued drop and relatively fast recovery in neutron counts that occur after saturation is reached during large rain storms, which may possibly be due to water that puddles/collects at the surface of the ground after saturation is reached and evaporates at a faster rate than the moisture down in the soil, and a two-day period from July 29 to July 31 during which the models consistently under predict the neutron counts measured. It is uncertain whether this two-day deviation is due to a weakness of the model or to some interesting neutron activity during the period.

To investigate the predictive capabilities of these models, they were fit to an earlier uninterrupted period of this campaign (June 23 to July 7) using the parameters acquired from the fit described above. Only the initial soil saturation fraction $M_0$ was allowed vary in these fits. Figs. 15–17 show the corrected $BF_3$ counts for this period (shown in blue circles) overlaid with least-squares fits of Models A (shown in red triangles), B (shown in green squares), and C (shown in magenta diamonds). Qualitatively, Model A does a poor job of reproducing this earlier data set. Models B and C perform better and produce mostly similar results.

To quantitatively compare the models, three different statistical quality measures were calculated: the coefficient of determination, the Nash-Sutcliffe efficiency, and the Willmott index of agreement. The first quantity, the coefficient of determination $R^2$, is simply the square of the Pearson product-moment correlation coefficient and measures the linear correlation between the observed values $O$ and the predicted values $P$. The values of $R^2$ range from 0 (no correlation) to 1 (perfect correlation) and are calculated as follows:

$$R^2 = \frac{\left(\sum_i \left(O_i - \overline{O}\right) \cdot \left(P_i - \overline{P}\right)\right)^2}{\left(\sum_i \left(O_i - \overline{O}\right)^2\right) \cdot \left(\sum_i \left(P_i - \overline{P}\right)^2\right)} = \frac{(cov(O,P))^2}{\sigma_O^2 \cdot \sigma_P^2} \tag{11}$$

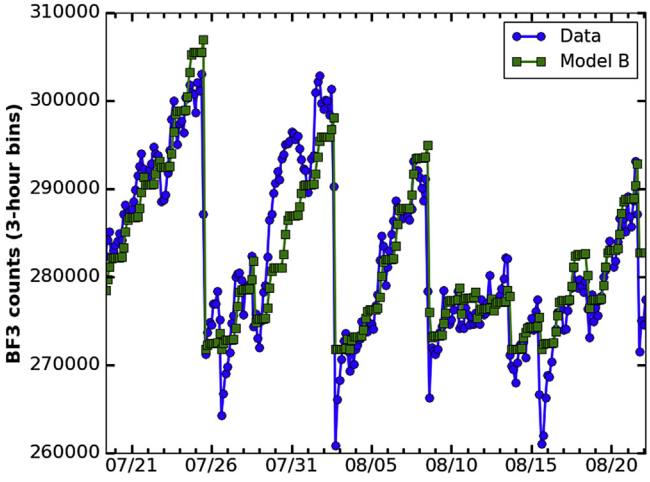


**Fig. 13.** Corrected counts (blue circles) and Model B (green squares) fit to data for longest uninterrupted data set for the $BF_3$ modules. (For interpretation of the references to colour in this figure legend, the reader is referred to the web version of this article.)

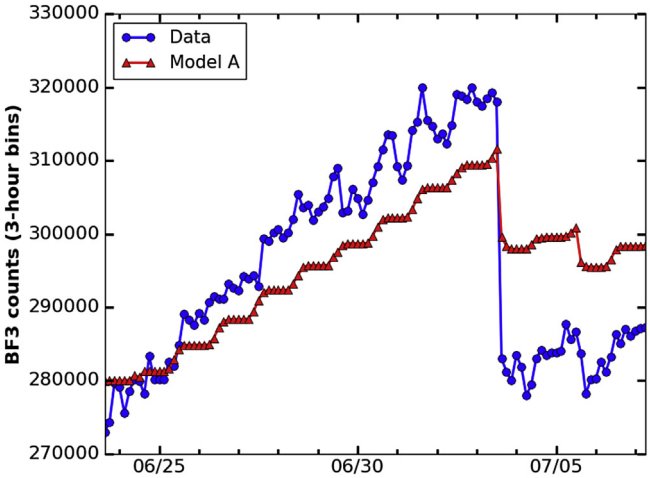


**Fig. 15.** Corrected counts (blue circles) and Model A (red triangles) fit to data for an earlier uninterrupted data set for the $BF_3$ modules. (For interpretation of the references to colour in this figure legend, the reader is referred to the web version of this article.)

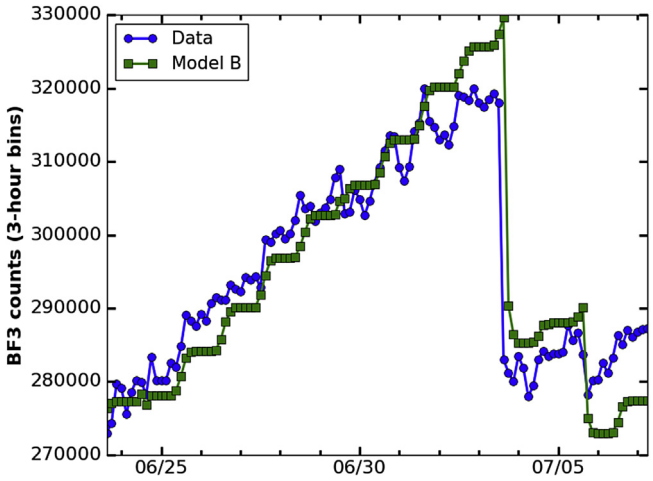


**Fig. 16.** Corrected counts (blue circles) and Model B (green squares) fit to data for an earlier uninterrupted data set for the $BF_3$ modules. (For interpretation of the references to colour in this figure legend, the reader is referred to the web version of this article.)

where $\overline{X}$ and $\sigma_X$ are, respectively, the mean and standard deviation for values $X$.

The Nash-Sutcliffe efficiency $E$ (Nash and Sutcliffe, 1970) assesses the predictive power of a model compared to the mean of the observed points. This coefficient ranges from $-\infty$ to 1 and is defined as

$$E = 1 - \frac{\sum_i (O_i - P_i)^2}{\sum_i \left(O_i - \overline{O}\right)^2} = 1 - \frac{MSE(O,P)}{\sigma_O^2} \tag{12}$$

where $MSE(O,P)$ is the mean squared error of $P$ with respect to $O$. An $E$ coefficient greater than 0 indicated that the model describes the data better than the mean, whereas a negative value for this coefficient indicates that the data are better described by the mean than by the model.

The index of agreement $d$ proposed by Willmott (Willmott et al., 1985) is similar to $E$ but ranges between 0 and 1 like $R^2$; $d$ is defined as follows:

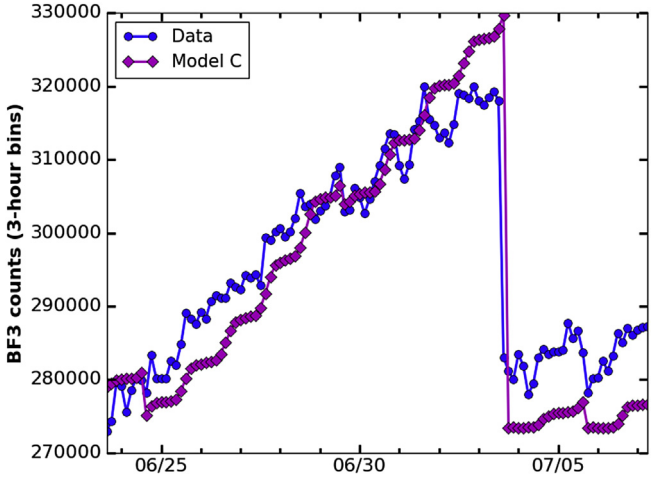


**Fig. 17.** Corrected counts (blue circles) and Model C (magenta diamonds) fit to data for an earlier uninterrupted data set for the $BF_3$ modules. (For interpretation of the references to colour in this figure legend, the reader is referred to the web version of this article.)

$$d = 1 - \frac{\sum_i (O_i - P_i)^2}{\sum_i \left(|P_i - \overline{O}| + |O_i - \overline{O}|\right)^2} \tag{13}$$

The calculated values of each statistical quality measure for the three models are given in Table 1 (for the July 19-August 22 data set) and Table 2 (for the June 23-July 7 data set). For almost all cases, Model B results in the best statistical quality values ($R^2$ is slightly higher for Model C in Table 2), whereas the values for Model A are consistently the worst. When the period of underprediction mentioned earlier (July 29 to July 31) are omitted from these calculations, the statistical quality measures only improve by 3–4%. Of particular interest is the fact that the values of $R^2$ and $E$ are equal (to three decimal places) for each of the models for the July 19-August 22 data set. Note that (Murphy and Epstein, 1989) (Weglarczyk, 1998)

$$E = R^2 - B_C^2 - B_U^2 \tag{14}$$

where $B_C^2$ and $B_U^2$ are, respectively, the conditional (nonsystematic) and unconditional (systematic) biases and are defined as follows:

$$B_C^2 = \left(\frac{\sigma_P}{\sigma_O} - R\right)^2 \tag{15}$$

$$B_U^2 = \frac{\left(\overline{P} - \overline{O}\right)^2}{\sigma_O^2} \tag{16}$$

If $E \approx R^2$, then $B_C^2 + B_U^2 \approx 0$; that is, the model has very low bias.

The parameters for the two more complex models, obtained from the least-squares fit, are given in Table 3. As may be expected from the similar results produced by the two models, the parameters are similar for Models B and C. The predicted fractional soil moisture $M$ based on the fit parameter values, which is shown in Fig. 18. Based on the values for these models, the soil moisture for this time period never falls below 94% saturated, although Model B predicts a slightly faster evaporation rate than does Model C. However, the similarity between the results for Models B and C reinforces the assumption that solar radiation dominates the evaporation term (at least for this location).

## 7. Conclusion

Background neutron rates were measured for a two-month period at the ICLRT located at Camp Blanding, FL, using a suite of moderated gas proportional detectors. These moderated detectors were most sensitive to neutron energies ranging from 0.1 eV to

**Table 1**
Statistical quality measures for the July 19-August 22 data set.

| Quantity | Model A | Model B | Model C |
|---|---|---|---|
| $R^2$ | 0.643 | 0.801 | 0.799 |
| $E$ | 0.643 | 0.801 | 0.799 |
| $d$ | 0.885 | 0.942 | 0.941 |

**Table 2**
Statistical quality measures for the June 23-July 7 data set.

| Quantity | Model A | Model B | Model C |
|---|---|---|---|
| $R^2$ | 0.494 | 0.840 | 0.862 |
| $E$ | 0.489 | 0.756 | 0.682 |
| $d$ | 0.794 | 0.949 | 0.940 |

**Table 3**
Parameters for the more complex models based on least-squares fit.

| Parameter | Model B | Model C | Units |
|---|---|---|---|
| $C_0$ | $2.08 \times 10^6$ | $2.37 \times 10^6$ | Neutrons/(3-h bin) |
| $M_0$ | 0.988 | 0.987 | Unitless |
| $k_0$ | 2.04 | 2.16 | Unitless |
| $k_1$ | $7.98 \times 10^{-2}$ | $1.78 \times 10^{-1}$ | $(\text{inches rainfall})^{-1}$ |
| $k_2$ | $1.52 \times 10^{-6}$ | $2.25 \times 10^{-4}$ | $m^2/J$ (Model B) or $mm^{-1}$ (Model C) |

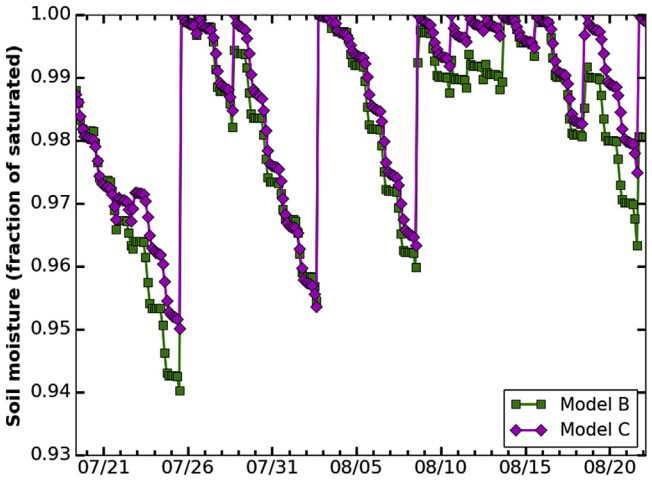


**Fig. 18.** Fractional soil moisture based on fit parameter values for Models B and C.

1 MeV. Variations in the measured neutron counts on the order of 10% were observed. The dominant cause of these variations was determined to be the changing moisture level of the surrounding soil; increasing soil moisture correlated to decreasing neutron counts.

Soil moisture levels can affect the magnitude of the local neutron background to a much larger degree than more well-known effects like atmospheric pressure or cosmic-ray rate variations. An accurate model to describe local neutron background variations based on easily measured climatological data would be invaluable to provide corrections for stationary neutron monitors. Relatively simple models, based only on the rainfall and solar irradiance in the area, were able to reproduce the major variations in our measured neutron counts with time. A more complex model using the CIMIS evapotranspiration equation reinforced the assumption that solar radiation is the dominant factor for evaporation for this data set. Remarkably, better performance was seen by assuming solar radiation dominated the evaporation process instead of using the more complex CIMIS equation. Further measurements to acquire data sets with longer periods of evaporation between rainfall events may help further refine the models.

## Acknowledgements

The authors of this work gratefully acknowledge the funding from the Chief of Naval Research (CNR). The authors also thank the management and staff at the International Center for Lightning Research and Testing for their hard work in supporting these measurements.

## Appendix

The CIMIS modified Penman equation calculates the potential evapotranspiration (i.e., the maximum evapotranspiration possible if moisture is present) for a grass reference. The following formulation was taken from the description of derived variables for Davis Instruments weather products (Instruments, 2006) and the Food and Agriculture Organization of the United Nations (Allen et al., 1998).

Define the following quantities:

$T_c$ : mean temperature in °C
$P$ : mean atmospheric pressure in kPa
$U$ : mean wind speed in m/s
$S$ : mean solar radiation in $W/m^2$
$H$ : mean relative humidity in percent

We can then calculate the following:

- Saturation water vapor pressure:

$$e_S = 0.6108 \cdot e^{\left(\frac{17.27 \cdot T_c}{T_c + 237.3}\right)}$$

- Actual water vapor pressure:

$$e_A = e_S \cdot \frac{H}{100}$$

- Slope of the saturation vapor curve:

$$\Delta = \frac{e_S}{T_c + 273.16} \cdot \left(\frac{6790.4985}{T_c + 273.16} - 5.02808\right)$$

- Psychrometric constant:

$$\gamma = 0.000646 \cdot P \cdot (1 + 0.000946 \cdot T_c)$$

- Radiation weighting factor:

$$W = \frac{\Delta}{\Delta + \gamma}$$

- Net solar radiation (for an albedo constant $\alpha = 0.23$):

$$S_N = (1 - \alpha) \cdot S$$

- Wind function:

$$F = \begin{cases} 0.030 + 0.0576 \cdot U \ (if\ S_N > 0) \\ 0.125 + 0.0439 \cdot U \ (if\ S_N = 0) \end{cases}$$

- Latent heat of vaporization:

$$\lambda = 694.5 \cdot (1 - 0.000946 \cdot T_c)$$

The potential evapotranspiration (in mm) can then be expressed as

$$E = W \cdot \frac{S_N}{\lambda} + (1 + W) \cdot (e_S - e_A) \cdot F$$

## References


Agonstinelli, S., et al., 2003. Geant4-a simulation toolkit. Nucl. Instrum. Methods Phys. Res. Sect. A Accel. Spectrom. Detect. Assoc. Equip. 506 (3), 250–300.

Allen, R.G., Pereira, L.S., Raes, D., Smith, M., 1998. Crop Evapotranspiration - Guidelines for Computing Crop Water Requirements. Food and Agriculture Organization of the United Nations, Rome.

Paschalis, P., et al., Athens cosmic ray station barometric coefficient form, [Online]. Available: http://cosray.phys.uoa.gr/index.php/data/nm-barometric-coefficient. (Accessed April 2016).

Grove, J.E., Johnson, W.N., Phlips, B.F., Wulf, E.A., Hutcheson, A.L., Mitchell, L.J., Woolf, R.S., Schaal, M., Uman, M.A., Jordan, D.M., Dwyer, J.R., 2014. Search for Neutrons Associated with Lightning Discharges, 2014 Fall Meeting. AGU, San Francisco, CA.

Hendrick, L.D., Edge, R.D., 1966. Cosmic-ray neutrons near the Earth. Phys. Rev. 145 (4), 1023–1025.

Hutcheson, A.L., Phlips, B.F., Wulf, E.A., Mitchell, L.J., Johnson, W.N., Leas, B.E., 2014. Maritime detection of radiological/nuclear threats with hybrid imaging system. In: Homeland Security Affairs, Vol. Supplement — 2014: IEEE 2013 Conference on Technology for Homeland Security. Best Papers, pp. 1–5.

Hutcheson, A.L., Phlips, B.F., Wulf, E.A., Mitchell, L.J., Woolf, R.S., 2015. Standoff detection of thermal and fast neutrons. In: Technologies for homeland security (HST), 2015 IEEE international symposium on. Waltham, MA.

Davis Instruments, 2006. Derived Variables in Davis Weather Products. Application Note 28. Davis Instruments, Hayward, CA.

Litvak, M.L., et al., 2008. The dynamic albedo of neutrons (DAN) experiment for NASA's 2009 Mars science laboratory. Astrobiology 8 (3), 605–612.

Mitrofanov, I.G., et al., 2010. Hydrogen mapping of the lunar south pole using the LRO neutron detector experiment LEND. Science 330 (6003), 483–486.

Murphy, A.H., Epstein, E.S., 1989. Skills scores and correlation coefficients in model verification. Mon. Weather Rev. 117, 572–581.

Nash, J.E., Sutcliffe, J.V., 1970. River flow forecasting through conceptual models Part I — a discussion of principles. J. Hydrology 10 (3), 282–290.

Natural Resource Conservation Service, 1989. Soil Survey of Clay County, Florida. United States Department of Agriculture, Washington, D.C.

Neutron Monitor Database, [Online]. Available: http://www.nmdb.eu. (Accessed April 2016).

Novikova, E.I., Strickman, M.S., Gwon, C., Phlips, B.F., Wulf, E.A., Fitzgerald, C., Waters, L.S., Johns, R.C., 2006. Designing SWORD – SoftWare for optimization of radiation detectors. In: 2006 IEEE Nuclear Science Symposium Conference Record. San Diego, CA.

Penman, H.L., 1948. Natural evaporation from open water, bare soil and grass. Proc. R. Soc. Lond. Ser. A, Math. Phys. 193 (1032), 120–145.

Snyder, R., Pruitt, W., 1985. California Irrigation Management Information System Final Report. Univ. of California-Davis, Davis, CA.

Weglarczyk, S., 1998. The interdependence and applicability of some statistical quality measures for hydrological models. J. Hydrology 206, 98–103.

Willmott, C.J., Ackleson, S.G., Davis, R.E., Feddema, J.J., Klink, K.M., Legates, D.R., O'Donnell, J., Rowe, C.M., 1985. Statistics for the evaluation and comparison of models. J. Geophys. Res. 90, 8995–9005.

Zreda, M., Shuttleworth, W.J., Zeng, X., Zweck, C., Desilets, D., Franz, T., Rosolem, R., 2012. COSMOS: the cosmic-ray soil moisture observing system. Hydrology Earth Sci. Syst. 16, 4079–4099.